Journal of Materials Chemistry A

Counterion condensation or lack of solvation? Understanding the activity of ions in thin film block copolymer electrolytes

Journal:	*Journal of Materials Chemistry A*
Manuscript ID	TA-ART-04-2020-004266.R2
Article Type:	Paper
Date Submitted by the Author:	04-Jun-2020
Complete List of Authors:	Lei, Qi; Louisiana State University, Cain Department of Chemical Engineering Li, Ke; Louisiana State University, Department of Chemistry Bhattacharya, Deepra; Louisiana State University, Cain Department of Chemical Engineering Xiao, Jingya; Louisiana State University, Cain Department of Chemical Engineering Kole, Subarna; Louisiana State University, Cain Department of Chemical Engineering Zhang, Qingteng; Argonne National Laboratory, X-ray Science Division Strzalka, Joseph; Argonne National Laboratory, X-Ray Science Division Lawrence, Jimmy; Louisiana State University Department of Chemistry, 3307 Patrick F. Taylor Hall Kumar, Revati; Louisiana State University, Chemistry Arges, Christopher; Louisiana State University, Cain Department of Chemical Engineering

ARTICLE

Counterion condensation or lack of solvation? Understanding the activity of ions in thin film block copolymer electrolytes

Qi Lei[a], Ke Li[b], Deepra Bhattacharya[a], Jingya Xiao[a], Subarna Kole[a], Qingteng Zhang[c], Joseph Strzalka[c], Jimmy Lawrence[a], Revati Kumar[b*], and Christopher G. Arges[a*]

Polymer electrolytes are found at the heart of numerous electrochemical technologies involved in energy storage, conversion and separations. An important property of these materials is their partitioning behavior of ions in aqueous solutions and its effect on the activity of the ions within the polymer electrolyte. In this work, the fraction of condensed counterions (f_c) were quantified in nanostructured block copolymer electrolyte (BCE) thin films with new and established experimental techniques. The transition between the osmotic-controlled regime and condensation-controlled regime in BCEs was identified using environmental GI-SAXS and solution uptake measurements via a quartz crystal microbalance (QCM). Further, the activity coefficients of ions in thin film BCEs were quantified experimentally and these values matched predictions from Manning's Theory of counterion condensation if the average distance between fixed charges on the polymer chains were determined accurately. Classical molecular dynamics simulations were also performed to assess counterion condensation and ionic conductivity values. The simulations showed large f_c values in the BCE – agreeing with results from GI-SAXS and QCM. Because a holistic approach was adopted, it was uncovered that f_c can vary significantly depending on the experimental method and analysis deployed. Interestingly, ionic conductivity measurements of the BCE thin films with aqueous solutions and humidified vapor revealed that solvation is critical for breaking ion pairs, and that the notion of two distinct counterion types, condensed and non-condensed, may not be the most accurate picture despite the utility of Manning's theory for accurately predicting the activity coefficient of ions in polymer electrolytes.

INTRODUCTION

Polymeric ion-exchange membranes (IEMs) are central components to electrochemical processes engaged in separations, electrolysis, and energy storage and conversion(1-3). IEMs are often interfaced with aqueous salt solutions and there is significant interest in understanding ion partitioning behavior between the IEMs and the liquid solutions from a molecular thermodynamics point of view(4). Furthermore, ionic conductivity and ion selectivity represent key bulk material properties that ultimately govern the efficiency of the aforementioned electrochemical processes(1). Ionic conductivity is inversely commensurate to the ohmic overpotential drop in electrochemical cells and thus there are significant incentives to boost ionic conductivity to improve the thermodynamic efficiency of electrochemical cells(5). Additionally, permselectivity for counterions and exclusion of co-ions have significant ramifications for the current utilization in electrochemical separations such as

[a]Cain Department of Chemical Engineering, Louisiana State University, Baton Rouge, LA 70803

[b]Department of Chemistry, Louisiana State University, Baton Rouge, LA 70803

[c]X-ray Sciences Division, Argonne National Laboratory, Lemont, IL 60439

*Corresponding author: carges@lsu.edu, kumar@lsu.edu

electrodialysis(6) and membrane capacitive deionization(7).

The molecular descriptors for the thermodynamics behind ion partitioning of IEMs and salt solutions, as well as ion transport phenomena in IEMs, has been an intense area of research(4, 8-14). Within the past 5 years, Freeman and co-workers(4, 12, 15, 16), as well as others(17), have applied Manning's Theory of counterion condensation to describe the thermodynamic partitioning behavior of salt solutions with IEMs. They have also used physics-based models with few fitting parameters to relate the condensation phenomena to co-ion and counterion diffusion within IEMs(13, 18-21). Although much progress has been made, there are still many open-ended questions about the counterion condensation phenomena and its role in selectivity and ionic conductivity in polymer electrolytes used in IEMs. For example, how does the molecular architecture, such as polymer electrolyte morphology, impact the extent of counterion condensation(13)? Does water structure within the material, as well as the ionic group chemistry (e.g., resonance structures or charge asymmetry), influence counterion condensation?

It is important to highlight that the majority of counterion condensation studies(12, 13, 16, 21, 22) in IEMs have been mostly limited to bulk IEMs that are amorphous, crosslinked and/or reinforced. There have been a few studies on counterion condensation in perfluorsulfonic acid membranes (PFSA, e.g., Nafion® and short side chain PFSAs)(17, 23), but these materials have a distribution of morphological geometries and the exact nature of their microphase separated structure at different levels of hydration is a subject of debate and an active area of research(24). Other counterion condensation studies have also examined polymer electrolytes dissolved in liquids(25-27) and polymer brushes(28-30).

Arges and co-workers(31-34) have recently adopted the tools of directed self-assembly (DSA) of block copolymers to prepare high fidelity nanostructured block copolymer electrolytes (BCEs) with systematically varied period sizes and with aligned and anti-aligned ionic grains to electrode surfaces. The DSA approach has provided unique insights that relate microstructure design of the BCE to bulk ionic conductivity properties. For example, perfectly aligned ionic grains in BCEs(34) to electrode surfaces, and with a tortuosity of 1, displayed 4 orders of magnitude greater ionic conductivity over anti-aligned ionic grains.

The advent of high fidelity BCE microstructures(36) enables robust studies that can correlate the extent of ionic dissociation in polymer electrolytes to ionic conductivity without having structural defects muddling interpretation of experimental results. The Freeman group has emphasized that there is a need to study counterion condensation in microphase separated IEMs(13) as the heterogenous design of these materials can offer desired mechanical properties while also enabling facile ion transport. Although the BCE studies by Arges and co-workers(31-34) were carried out in a thin film format (10 to 100 nm), the microstructures observed in thin films mimic the structures (e.g., lamellae, cylinders, and gyroids) observed in BCE type membranes(37). Hence, thin film BCEs are excellent model systems that can be systematically tuned in their morphology, period size, and alignment through the litany of controlled living polymerization methods(38) and the tools of DSA(39). Plus, thin film studies require small quantities of materials making it possible to study counterion condensation in a multitude of polymer electrolyte structures and chemistries without being burdened with large-scale syntheses.

This report disseminates experimental, theoretical, and molecular simulation approaches for examining ion activity in nanostructured BCE thin films and quantifying counterion condensation. The selection of poly(styrene-*block*-2-vinyl pyridine-*co*-n-methyl pyridinium iodide) (PS*b*P2VP/NMP^+ I^-) as the BCE was based upon previous works by Arges *et al(31, 32, 34)* that converts the non-ionic variant of this material, poly(styrene-*block*-2-vinyl pyridine) (PS*b*P2VP), post self-assembly into a BCE with long-range order. PS*b*P2VP is a block copolymer that has an excellent track record to make straight-line lamellae over large areas using the principles of DSA(35). The selection of a lamellae microstructure for the BCE allowed the use of top-down metrology tools, like scanning electron microscopy (SEM),

and grazing incidence small-angle x-ray scattering (GI-SAXS) for characterization.

In this work, several experimental techniques, environmental GI-SAXS, solution uptake using quartz crystal microbalance (QCM), and thin film ionic conductivity measurements on interdigitated electrodes (IDEs), were effective for identifying the external solution transition point (C_{tp}) that marked when the BCE moved from the osmotic-controlled regime to the condensed-controlled regime. This transition point(14, 28), sometimes referred to as the Donnan concentration, has been used for quantifying counterion condensation in solid polymer electrolytes. Similar to the work by Balsara and co-workers[13], this work shows that the Donnan concentration gives an extremely high fraction of condensed counterions (f_c) when compared to other techniques(4, 12). Alternatively, f_c was determined by measuring the activity coefficients of the ions in the BCE thin films. The measured activity coefficients were compared against predictions using Manning's Theory of counterion condensation(40) and agreement was observed between experiments and predictions provided the average distance between fixed charges within the BCE were used. Notably, f_c was smaller when using Manning's Theory of counterion condensation and the Gibbs-Donnan model. Classical molecular dynamics (MD) simulations were also deployed to examine the condensation effect of ions in model BCEs and these simulations showed large extents of counterion condensation – similar to what was observed in GI-SAXS and QCM experiments that relied upon the identification of C_{tp}. Finally, ionic conductivity measurements of BCE thin films with and without adsorbed salt conveyed the importance of hydration on dissociating ion pairs and promoting conductivity. The observations from ionic conductivity experiments, and the results from the Gibbs-Donnan equilibrium model, suggest that solvation is an important descriptor for ion activity in polymer electrolytes and ionic conductivity.

EXPERIMENTAL DETAILS

The SI lists all materials and procedures used to prepare BCE thin films with perpendicular alignment on silicon wafer and IDEs following the established procedures by Arges *et al.*(31-34) This includes SEM imaging and EIS for ionic conductivity measurements. This work used OH-terminated random copolymer brush was synthesized via reversible addition fragmentation chain transfer (RAFT, see SI section(41)). The reported experimental techniques and MD simulations to study counterion condensation is given below.

The solution uptake (SU) for BCE films immersed with KI_{aq} were measured using a Gamry e-chem QCM. The PS*b*P2VP/NMP$^+$ I^- BCE thin films were self-assembled on gold quartz crystals using the same procedure for Si wafers(31-34). The quartz crystal with the BCE was loaded into the QCM and chamber and then an KI_{aq} solution, or 95 % relative humidity, was passed across the sample and the frequency shift of the polymer was monitored. The frequency shift was converted into mass gain using **equation 1**(42). The mass gain was used to determine the swelling uptake and λ using **equations 2** and **3**(43). All experiments were conducted at 22 to 25 °C.

$$\Delta f = - C_f \bullet \Delta m \quad <1>$$

Δf: the observed frequency change (Hz)
Δm: the change in mass per unit area, in g cm^{-2}
C_f: the sensitivity factor for the crystal used (e.g., 226 Hz μg^{-1} cm^2 for a 5 MHz Au coated quartz crystal at room temperature)

$$SU = \frac{W_{\text{hydrated}} - W_{dry}}{W_{dry}} \quad <2>$$

$$\lambda = \frac{(W_{\text{hydrated}} - W_{dry})/MW}{IEC \cdot W_{dry}} = \frac{SU}{IEC * MW} \quad <3>$$

GI-SAXS experiments were performed at the Advanced Photon Source (APS) Sector Beamline 8-ID-E at Argonne National Laboratory. The beamline was equipped with an environmental chamber and a humidity control system. BCE thin films on Si wafer, with and without KI_{aq} droplets, were measured at the same humidity (95%). Humidity was applied with experiments featuring liquid droplets to prevent the droplet from evaporating. The grazing incidence angle was 0.14 ° for dry samples and 0.11 ° for samples with a droplet on it. All GI-SAXS data were analyzed using the GIXSGUI(44, 45) software

package from APS to obtain GISAXS intensity and integrate a region of the 2D data along q_z, the out-of-plane direction, to get the intensity as a function of q_y, the in-plane direction (**equation 4(45)**)

$$q_{x,y,z} = \frac{2\pi}{\lambda}\begin{bmatrix}\cos(\alpha_f)\cos(2\theta_f) - \cos(\alpha_i)\\ \cos(\alpha_f)\sin(2\theta_f)\\ \sin(\alpha_f) + \sin(\alpha_i)\end{bmatrix} \quad <4>$$

Where α_i is the incident angle, α_f is the exit angle of the scattered photo, θ_f is the in-plane scattering angle, λ is the x-ray wavelength, 1.136 Å (10.91 keV).

The counterion and co-ion concentration in the thin films was measured using ion sorption experiments. BCE samples were prepared on 1-inch diameter Si wafers. Then, the sample was loaded into plexiglass cell that could be sealed and had an injection port (**Figure S2c**). Then, 0.5 mL KI_{aq} solution was placed on the surface of the wafer with the BCE sample. After 24 hours, the KI solution was syringed out and 1mL of DI water was injected into the chamber and placed on top of the BCE sample. The DI water was interfaced with the BCE sample for 24 hours and then syringed out and transferred to a glass vial. The concentration of K^+ was quantified using ICP-OES. The signal response from ICP-OES was related to the concentration of K^+ using a calibration curve (**Figure S9**). Note: All syringes for adding solutions and removing solutions used a 0.45 µm PTFE filter.

For determining the concentration of I^- in the BCE thin films, the samples were immersed in 5mL DMF solution after interacting them with KI_{aq} and removing that solution. The chamber with DMF on top of the BCE sample was sonicated for 10 minutes to dissolve all the polymer into the solvent. The iodide concentration was measured using LCMS. **Figure S10** gives the calibration curve for I^- concentration and the LCMS instrument response.

The same procedure for placing BCEs on silicon wafers was followed for placing BCEs on IDE substrates(31, 32). The IDE samples with the PS*b*P2VP/NMP^+ I^- BCE samples were placed in a home-built stainless-steel chamber that had temperature and humidity control and that could be sealed (**Figure S6b**). Further, this chamber had a temperature probe and electrical contacts for making ionic conductivity measurements for the BCE on IDEs. For liquid droplet conductivity measurements, the liquid droplet was placed on the IDE in the sealed chamber. 95% RH with a nitrogen carrier gas was delivered to the testing chamber at 1 L min^{-1} through control of the dew point temperature on the bubbler. Both of these sets of measurement were carried out at room temperature (22 to 25 °C). The BCE film resistance was determined using electrochemical impedance spectroscopy (EIS) carried out in galvanostatic mode (see SI for details) (31, 32).

Simulations were performed using a conventional, non-reactive force field based on OPLSAA(46) with the TIP3P(47) water model using the LAMMPS(48) program. A model BCE 40-mer was chosen with a hydrophobic (styrene) segment followed by hydrophilic segment of equal length with the hydrophilic segment consisting of alternating charged (pyridinium) and unchanged (pyridine) segments (**Figure S11**). For each tethered positively charged pyridinium moiety, an iodide counterion was introduced. To mimic the experimental conditions, 30 chains were solvated with water in a cubic box with a box length around 100 Å. The water amount was based on the experimental data from solution uptakes experiments - which determined 6 water molecules per pyridinium group. Four separate sets of simulations were carried out, one without added KI salt, the others with KI salt added. The ratio of water to KI added was 1: 300, 1: 45, 1: 20, respectively in the latter three sets of simulations. Replica exchange MD simulations were carried out for enhanced sampling to determine structural data followed by canonical simulations in the isothermal ensemble to determine dynamical data. Non-equilibrium simulations in the presence of an electric field of 0.1 V $Å^{-1}$ in the z direction were carried out to determine ionic conductivities. The complete details of the simulation protocol, from force-field details to setup and equilibration, can be found in the SI section (**Figures S13 - S15** and **Tables S1** and **S2**).

RESULTS AND DISCUSSION

Figure 1a depicts the process to make a nanostructured BCE of PS*b*P2VP/NMP^+ I^- on a silicon wafer substrate. The ionic and non-ionic block domains in the PS*b*P2VP/NMP^+ I^- sample were aligned perpendicular to the substrate surface for assessing BCE's morphology

using SEM and for GI-SAXS characterization of the BCE sample when interfaced with aqueous salt droplets that would swell or de-swell the ionic domains. Orienting the ionic domains at the interface ensured that the aqueous salt solution could assess the hydrophilic domains of the BCE film.

Figures 1b and **1c** are the electron micrograph and the 2D GI-SAXS scattering pattern of PS*b*P2VP/NMP$^+$ I$^-$. Both the electron micrography (Fast Fourier Transform - FFT) and GI-SAXS scattering pattern, analyzed by the Yoneda peaks(31), revealed that this BCE under 20% relative humidity at 20 °C had a natural period of 44 nm. The SEM image conveys that PS*b*P2VP/NMP$^+$ I$^-$ had its polymer block domains aligned to the substrate surface because a fingerprint like lamellae structure was observed.

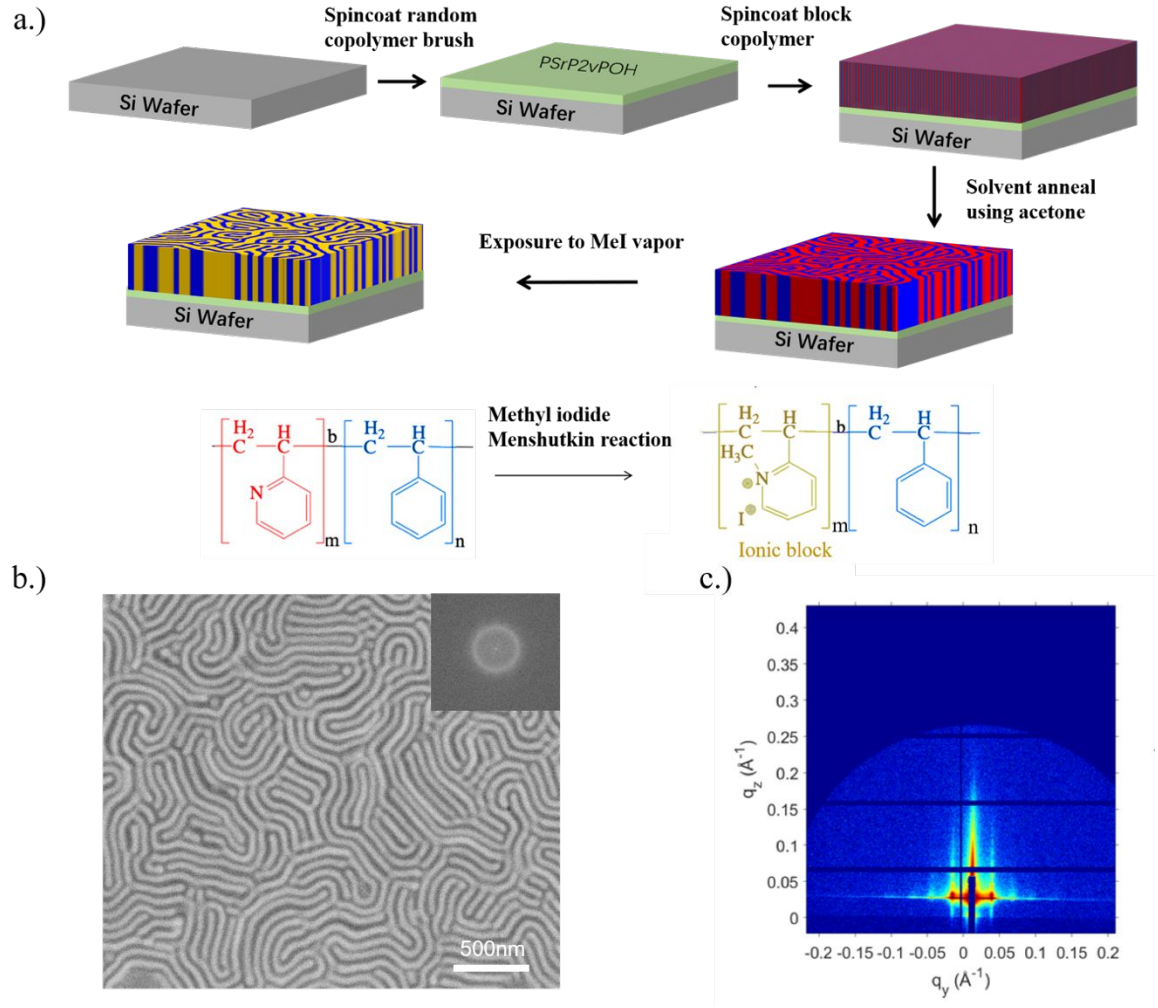

Figure 1. a.) Scheme to prepare nanostructured BCE thin films and Menshutkin reaction to prepare PS*b*P2VP/NMP$^+$ I$^-$, b.) electron micrograph of PS*b*P2VP/NMP$^+$ I$^-$, with FFT, L_0 = 44 nm c.) GI-SAXS scattering pattern of the same BCE in air environment. The Yoneda peaks from the scattering pattern demonstrate that the BCE has a 44 nm periodic spacing.

Balsara and co-workers(14) quantified the extent of counterion condensation in polymer electrolyte membranes through determination of C_{tp} via solution uptake measurements of Nafion® when interfacing the membrane with hydrochloric acid (HCl) solutions. As the external salt solution concentration increased, the bulk Nafion® membrane went from a constant solution uptake value to reduced solution uptake values. The external solution concentration value that marked the transition from a constant solution uptake to the start of a decreased solution uptake represented the C_{tp}. This transition point is important because it marks the activity of ions in solution that is needed to exceed the osmotic pressure within the polymer electrolyte causing

deswelling. Hence, the aqueous salt concentration values below C_{tp} signify that the polymer electrolyte is in the osmotic-controlled regime, while aqueous salt concentration values above C_{tp} indicate that the polymer electrolyte is in the condensation-controlled regime.

The BCE films in this report are sub-100 nm and have a small mass value. To identify the C_{tp} in thin films via solution, a QCM technique was deployed to monitor small changes in mass uptake when interfacing the films with different salt solutions. **Figure 2a** depicts the frequency change of polystyrene (PS) and PS*b*P2VP/NMP$^+$ I$^-$ BCE thin film in dilute aqueous potassium iodide (KI) solutions. As expected, the frequency change is substantially greater for the PS*b*P2VP/NMP$^+$ I$^-$ thin film versus the PS thin film because the BCE thin film contains hydrophilic ionomer blocks that are conducive for absorbing the aqueous electrolyte.

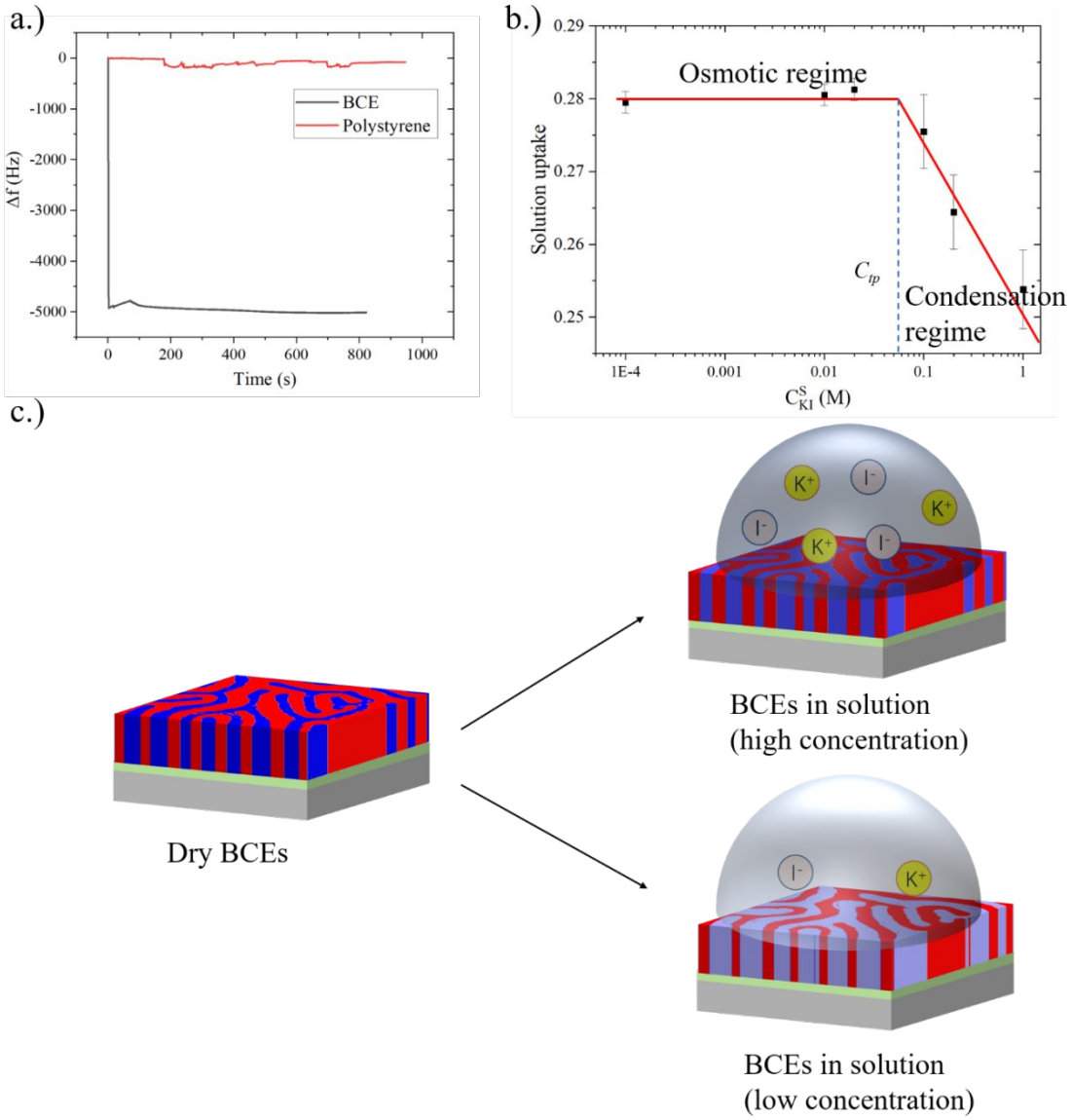

Figure 2. a.) Frequency change versus time using a QCM for polystyrene and a BCE PS*b*P2VP/NMP$^+$ I$^-$ thin film immersed in 1 M KI_{aq} solution. The frequency shift was used to determine the solution uptake values; b.) Solution uptake values (average for n=3 with standard error bars) of the BCE thin film as function of external KI_{aq} concentration. The C_{tp} was identified by the intersection of lines from constant solution uptake and the reduction in solution uptake. The C_{tp} marks the transition between the osmotic-controlled regime and the condensation-controlled regime. c.) An illustration of lamellae BCE thin film swelling and deswelling due to differences in the external KI_{aq} concentration.

Figure 2b shows the solution uptake for PS*b*P2VP/NMP$^+$ I$^-$ exposed to different concentrations of KI_{aq}. The solution uptake calculated from the frequency shift(49) (**Figure 2a**) was constant at dilute concentration values of KI_{aq} (< 0.03M). Increasing the KI_{aq} concentration beyond 0.03 M resulted in a continued decrease in the solution uptake of the BCE thin film. **Figure 2b** fits two independent lines for the constant solution uptake values and the linearly decreasing swelling uptake values versus $\log_{10}C_{KI}$. The intersection of these lines occurred at 0.055 ± 0.005 M KI_{aq} – which was the C_{tp}. Note: The error bar represents the standard error for n=3.

Figures 2a and **2b** demonstrate that QCM was effective for determining the C_{tp} in thin film BCEs. KI_{aq} below C_{tp} demonstrated that the PS*b*P2VP/NMP$^+$ I$^-$ thin film was in the osmotic-controlled regime indicating that the concentration of ions inside the thin film exceeded that of the external KI_{aq} solution resulting in the BCE film trying to adsorb as much water as possible to dilute the fixed charge carriers. Increasing the KI concentration in the external solution pass the C_{tp} value resulted in the PS*b*P2VP/NMP$^+$ I$^-$ thin film transitioning to the condensation regime. In this regime, the external solutions' osmotic pressure is greater than the film causing water withdrawal and a reduction in mass uptake. In previous reports(14, 28), C_{tp} was used to quantify f_c through **equation 5** (28)

$$f_c = 1 - \frac{C_{tp}}{C_{IEC}} \qquad <5>$$

C_{IEC}: concentration of fixed ion groups (i.e., ion-exchange capacity (IEC)) in the BCE (M)

Using **equation 5** and the measured C_{tp} would result in 97% of the counterions in PS*b*P2VP/NMP$^+$ I$^-$ thin films being condensed – which is similar to the 98% of counterions condensed observed in Nafion® via a similar approach(14). It is worth noting that **equation 5** only estimates f_c in the osmotic-controlled regime.

Another experimental method used to identify C_{tp} is small-angle x-ray scattering(23) (SAXS). Because the material of interest in this report deals with thin films rather than bulk membranes, an environmental GI-SAXS technique (**Figures S1a** and **S1b**) was developed to monitor shifts in the BCE periodic spacing with a liquid aqueous salt droplet on top of the nanostructured thin film. **Figure 3a** shows the 2D x-ray scattering pattern for the PS*b*P2VP/NMP$^+$ I$^-$ BCE thin film with a liquid droplet on it. The shadow of the liquid droplet on the thin film BCE was observed in the scattering pattern. Unlike **Figure 1c** that showed 4 Bragg diffraction peaks of equal q-spacing, the BCE thin film with a liquid droplet only showed two Bragg diffraction peaks (**Figure S1c**) because of x-ray attenuation by the liquid. However, obfuscation of the x-rays by the liquid droplet did not prevent monitoring changes in the periodic spacing of the 1st order Bragg diffraction peak when interfaced with KI_{aq} solutions of varying concentration (**Figure 3b**).

Figure 3c plots the Bragg diffraction peak spacing versus q_y as a function of KI_{aq} concentration. From this Figure, the q-spacing was larger for the sample immersed in the highest KI_{aq} concentration when compared to the sample immersed in the lowest concentration. Similar to the QCM experiments, the domain spacing ($L_0 = 2\pi/q$) is constant (L_0 = 45.5 nm) at dilute KI_{aq} concentrations and starts to decrease when changing the solution concentration from 0.03 M to 0.1 M. Using the same linear analysis that determined C_{tp} in **Figure 2b**, the C_{tp} value determined from GI-SAXS experiments was 0.060 ± 0.005 M. This value was very close to the value identified from QCM (0.055 ± 0.005 M). The C_{tp} value from GI-SAXS corresponded to a f_c of 97% if using **equation 5** – an identical value attained from QCM experiments.

An unresolved issue in the area of counterion condensation for IEMs pertains to how nanoscale architectures impact dissociated ion pairs and ion transport. Block copolymers can be systematically varied to control morphology and periodic feature sizes through controlled-living polymerization(38). **Figures 3a-c** unequivocally demonstrates that environmental GI-SAXS can be used to monitor shifts in the periodic spacing of BCE thin films with liquid supporting electrolyte on top. It is envisioned that the developed environmental GI-SAXS could also be useful for understanding ion partitioning and solution uptake effects with nanostructured polymer electrolyte materials interfaced with concentrated electrolytes – which is relevant for redox flow batteries(50). Despite that estimating f_c through measuring C_{tp} often gives very high extents of

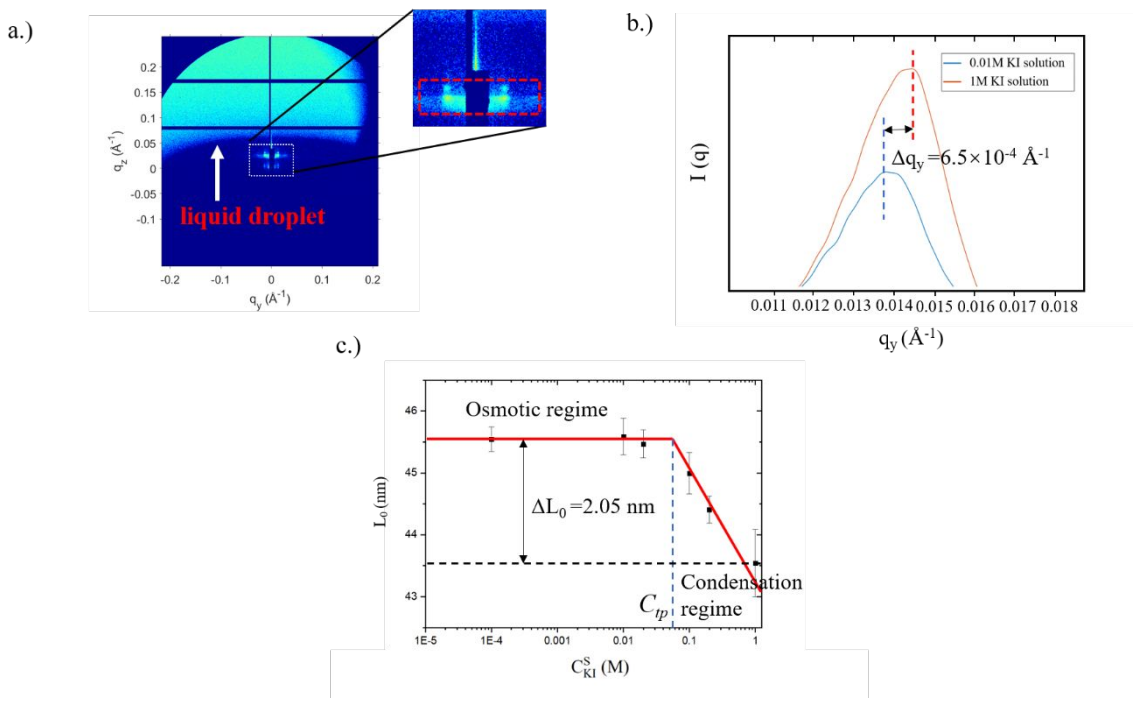

Figure 3. a.) GI-SAXS scattering pattern from BCE with a liquid KI_{aq} droplet on it. b.) Plots of GI-SAXS intensity (I) versus in-plane component of the scattering vector (q_y) of PS*b*P2VP/NMP$^+$ I$^-$ BCEs in contact with KI_{aq} of varying concentration. Curves are shifted vertically for clarity. c.) Calculated d-spacing values (average for n=3 with standard error bars) of the PS*b*P2VP/NMP$^+$ I$^-$ BCE thin film as function of external KI_{aq} concentration and the identification of C_{tp}.

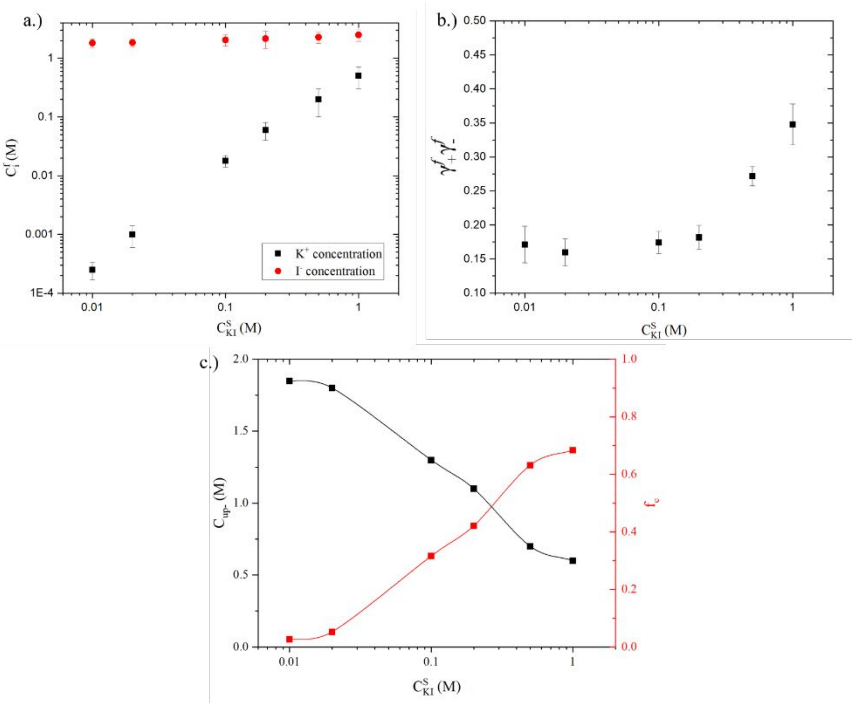

Figure 4. a.) Co-ion and counterion concentration values in the PS*b*P2VP/NMP$^+$ I$^-$ BCE thin films as a function of external KI_{aq} concentration. b.) Measured activity coefficients ($\gamma^f_+\gamma^f_-$) of counterion and co-ions in the BCE thin film. c.) The concentration of uncondensed counterions (C_{up}-) along the polymer chain in the BCE film (left y-axis) as a function of external KI_{aq} concentration. C_{up}- was determined from the Gibbs-Donnan equilibrium expression (**equation 7**) and by knowing $\gamma^f_+\gamma^f_-$. f_c in the BCE was calculated using **equation 8** and knowing C_{up}-.

condensation that is at odds with other methods(4, 12), the identification of C_{tp} is useful because it allows one to determine when film deswelling may occur. Plus, it could be a useful assessment tool to downselect new BCE materials that extends C_{tp} to larger values – i.e., more permselective IEM materials.

Previously, the transition between the osmotic-controlled regime and the condensed-controlled regime in BCE films has been determined using solution uptake values from QCM experiments and GI-SAXS experiments. These methods gave f_c values that were very large (97 %). Two additional experimental precedents for calculating f_c relied upon: i.) fitting either counterion release from adsorbed co-ions to the Gibbs-Donnan equilibrium model(23) and ii.) fitting experimentally determined activity coefficient models to Manning's Theory of counterion condensation(4). Both of these methods have been adopted in this work and it necessitated measurement of the co-ion concentration and counterion concentration in thin film BCEs exposed to KI_{aq} solutions. The co-ion sorption procedure is illustrated in **Figure S2a**. This procedure placed the KI_{aq} solution on the PS*b*P2VP/NMP^+ I^- thin film followed by equilibration and rinsing with DI water to extract the absorbed co-ions and then quantification of the amount of K^+ ions using ICP-OES. **Figure S2b** depicts the procedure for assaying counterion sorption into the PS*b*P2VP/NMP^+ I^- thin film. This procedure dissolved the thin film BCE with N, N-dimethylformamide (DMF) after exposure to KI_{aq} solution. The dissolved film was analyzed by LCMS to quantify the amount of I^- counteranions. **Figure S2c** shows the unique ion sorption chamber for thin film BCEs. Note: PS*b*P2VP/NMP^+ I^- thin films not exposed to KI_{aq} solutions were dissolved in DMF to determine the concentration of I^- in the film.

Figure 4a presents the co-ion and counterion concentration values in the PS*b*P2VP/NMP^+ I^- thin film after exposure to different external KI_{aq} solution concentrations. The co-ion concentration (K^+) rapidly rises when increasing the external KI_{aq} solution concentration. Conversely, the rise in concentration of the I^- counterion in the film after interfacing with KI_{aq} solutions is comparatively small. The small change in I^- concentration was attributed to the small amount of co-ion entering the BCE film due to Donnan exclusion and the already large I^- concentration present from the BCE.

Using the concentration of ions in the BCE film data presented in **Figure 4a**, it was possible to determine the activity coefficients of these ions using **equation 6** (4). The activity coefficients of the ions in the BCE film required knowing the activity coefficients of the ions in the external salt solution, attained from the literature(51) (**Figure S3**), as well as the concentration of ions in the liquid solution.

$$\gamma^f_+ \gamma^f_- = \frac{(\gamma^s_\pm)^2 (C^s_s)^2}{(C^f_+ C^f_-)} \quad <6>$$

$\gamma^f_+ \gamma^f_-$: the activity coefficients of the cations and anions in the thin BCE film

$\gamma^s_\pm$: the mean activity coefficient value of KI salt dissolved in water

C^s_S: the concentration of KI salt dissolved in water

Figure 4b presents the measured $\gamma^f_+ \gamma^f_-$ values for the PS*b*P2VP/NMP^+ I^- BCE thin film. The activity coefficient of the ions in the BCEs are very low and rise with increasing external solution concentration - similar to the literature(4). The low activity coefficients observed at low KI_{aq} hail from the large ionic concentration difference between the external solution and the BCE. Because of the glassy styrene block in the BCE film, the thin film cannot absorb enough water to dilute its fixed charge carriers to match the activity of ions in solution. Hence, the activity coefficient values of the ions in the BCE thin films are quite low. Increasing the external solution concentration led to smaller concentration difference between ions in the solution and BCE, and as a result, the activity coefficient of the ions in the BCE film increased.

With the activity coefficient values of the ions in the BCE film determined, as well as the co-ion adsorbed salt concentration values, the concentration of non-condensed counterions in the BCE (C_{up-}) was calculated using the Gibbs-Donnan equilibrium model (**equation 7** (3)).

$$C^f_+ = \frac{-C_{up-} + \sqrt{(C_{up-})^2 + 4\frac{(\gamma^s_\pm)^2}{\gamma^f_+\gamma^f_-}(C^s_s)^2}}{2} =$$

$$\frac{-C_{up-} + \sqrt{(C_{up-})^2 + 4\Gamma\cdot(C^s_s)^2}}{2} \quad <7>$$

C^f_+: concentration of K^+ in the BCE film

Γ: $\frac{(\gamma^s_\pm)^2}{\gamma^f_+\gamma^f_-}$

Figure 4c shows the calculated C_{up-} values for each KI_{aq} (i.e., C^s_s). The C_{up-} term is relatively constant below < 0.05 M KI_{aq} - providing further evidence that the BCE film is in the osmotic-controlled regime. Increasing KI_{aq} further resulted in a reduction of C_{up-} signaling that the film has entered the condensation-controlled regime.

By calculating C_{up-}, it was possible to determine f_c using **equation 8** – which is similar to **equation 5** but C_{tp} has been substituted with C_{up-}.

$$f_c = 1 - \frac{C_{up-}}{C_{IEC}} \quad <8>$$

The f_c determined from C_{up-} and **equation 8** is plotted in **Figure 4c**. This Figure shows that the extent of counterion condensation is almost negligible at low KI_{aq} and increases to 64% at 1 M KI_{aq}. Notably, this method for determining f_c leads to values that are significantly lower than using C_{tp} and **equation 5**.

The implications of f_c in **Figure 4c** implies that the BCE thin film has almost all of its fixed charges attempting to become dissociated through water uptake and solvation. In other words, almost all of the fixed charge-counterion pairs along the polymer backbone are exerting some level of activity. However, the extent of dissociation and exertion of activity ions in the BCE films is regulated by the water uptake – which is not enough due to the hydrophobic, glassy polystyrene polymer that prevents the BCE film from being dissolved. Although C_{up-} is high at low KI_{aq}, the activity of ions in the BCE film is small due to the low activity coefficient values. Increasing KI_{aq} past C_{tp} transitions the BCE film into the condensation-controlled regime. In this regime, the adsorption of salt within the film screens fixed charges and counterions along the polymer backbone leading to condensation (i.e., fixed charge-counterion pairs not contributing to activity) and a reduction in C_{up-}. The screening of fixed charges also explains why the co-ions are adsorbed; otherwise, Donnan exclusion and fully dissociated ion-pairs would mitigate co-ion adsorption.

The previous section showed the utility of knowing the $\gamma^f_+\gamma^f_-$ values in the BCE film with the Gibbs-Donnan equation for quantifying counterion condensation. It has been shown(4, 12, 13, 21) that Manning's Theory of counterion condensation (**equation 9** (4)) can predict the activity coefficients of ions in IEMs with no adjustable parameters and by knowing the Manning parameter (ξ) – which is the dimensionless variable of the Bjerrum length (λ_b) divided by the average distance between fixed charges along the polymer chain ('b') (**equation 10** (4)).

$$\gamma^f_+\gamma^f_- = \left(\frac{\frac{X}{\xi}+1}{X+1}\right)exp\left(\frac{-X}{X+2\xi}\right) \quad <9>$$

$$X = C_{IEC}/C^f_+$$

$$\xi = \frac{e^2}{4\pi\varepsilon_0\varepsilon kTb} = \frac{\lambda_B}{b} \quad <10>$$

e: protonic charge

ε: dielectric constant

ε_0: vacuum permittivity constant

kT: thermal energy of the system

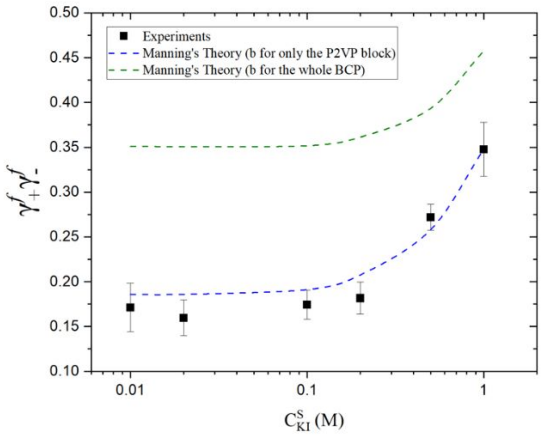

Figure 5. $\gamma^f_+\gamma^f_-$ predicted from Manning's Theory of counterion condensation with different average distance between fixed charges ('b') and compared against data from **Figure 4b**.

Using **equations 9** and **10**, **Figure 5** shows that Manning's Theory can accurately predict the measured

$\gamma^f_+ \gamma^f_-$ for the PS*b*P2VP/NMP$^+$ I$^-$ BCE provided that the average distance between fixed charges is approximated correctly. Normally, previous reports have estimated 'b' by taking the statistical length of the polymer chain (**equation S1** (4)) and dividing it by the number of fixed charge groups. However, because a BCE has a distinct microphase separated regime with agglomerated ionomer blocks and non-charged polymer blocks (i.e., polystyrene), the conventional approach for determining 'b' leads to inaccurate predicted $\gamma^f_+ \gamma^f_-$ values (the green trace in **Figure 5**). Reparametrizing 'b' by only determining the length of the ionomer block divided by the number of fixed charge groups led to predicted $\gamma^f_+ \gamma^f_-$ values that matched the measured values (the blue trace in **Figure 5**). Additionally, it is worth noting that the ξ value was not constant in the BCE interfaced with different KI_{aq}. The ξ value was determined in the BCE sample as function of the external KI_{aq} value (**Figure S4**) because the external solution concentration affected the solution uptake value leading to a change in the ε value. Hence, appropriate determination of ε (**equations S2a** and **S2b**)(52) and 'b' were vital for predicting the activity coefficient of ions in the BCE film using Manning's Theory.

Manning's Theory of counterion condensation posits that a linear polymer chain with fixed charge points along the line will condense its ions if ξ > 1 (i.e., ξ_{crit} = 1 for a monovalent salt). The theory proposes that a dense concentration of fixed charges along the polymer chain causes 'b' being small relative to λ_b (i.e., $\xi > \xi_{crit}$) fostering condensed counterions that do not exert activity. With this logic, Manning presents that $C_{up\text{-}}$ can be determined by C_{IEC}/ξ and that f_c is calculated using **equation 11** (21) – which is slightly differently than **equations 5** and **8** as it includes the counterion concentration contribution from co-ion adsorption.

$$f_c = 1 - \frac{\frac{C_{IEC}}{\xi} + C^f_+}{C_{IEC} + C^f_+} = 1 - \frac{\frac{X}{\xi} + 1}{X + 1} \qquad <11>$$

f_c ranges from 46 to 57 % when using **equation 11**. The differences in f_c between **equations 5**, **8**, and **11** will be discussed in greater detail after the presentation of molecular dynamics (MD) simulations and ionic conductivity measurements.

Classical MD simulations were performed to complement experimental results that quantified the extent of counterion condensation in microphase separated BCE chains. The MD simulations utilized 30 BCE chains in a box that contained 6 water molecules per n-methyl pyridinium iodide group along the polymer chain (**Figure 6a**). The water amount was informed from QCM experiments. The amount of n-methyl pyridinium iodide groups in the simulated BCEs were determined from the experimental approach shown in **Figure S2b**. Additionally, MD simulations were performed with the BCE chains featuring added KI salt. The amount of added KI to the BCE chains in the simulations were also informed from co-ion adsorption experimental data.

The MD simulations determined the proximity of the iodide ion to the tethered n-methyl pyridinium charge. The simulations give a direct measurement of ion pairing using the corresponding radial distribution (g(r)) function between the iodide ion and the carbon atom in the -CH_3 group bonded to the quaternarized nitrogen in n-methyl pyridinium along the polymer backbone. The first minimum in g(r) (**Figure 6b)** defines the first solvation shell of pyridinium around the iodide ion. The cumulative number density, n(r), (**Figure 6b**) is given by:

$$n(r) = \int_0^r 4\pi r^2 \rho g(r) dr \qquad <12>$$

The value of n(r) at the first minimum gives the average number of pyridinium ions solvated to an iodide in its first solvation shell. Hence the first minimum of g(r) is a robust definition of whether an iodide is condensed on the pyridinium or not. In other words, an iodide ion is taken to be condensed if the distance between the iodide ion and the C atom of the methyl group of the pyridinium is less than the cutoff. Inspection of **Figure 6b** demonstrates that a large fraction of counterions were condensed. This g(r) corresponded to a simulation that had no added KI salt.

Figure 7 reports the f_c values for the MD simulations that featured adsorbed KI salt and the experimentally determined values from **equations 5**, **8**, and **11**. As seen in previous experiments with **equations 8** and **11** (i.e., Gibbs-Donnan approach and Manning approach), the addition of adsorbed salt in MD simulations leads to more counterion

condensation. Another apparent observation in **Figure 7** is that the f_c values from the MD simulations were similar to

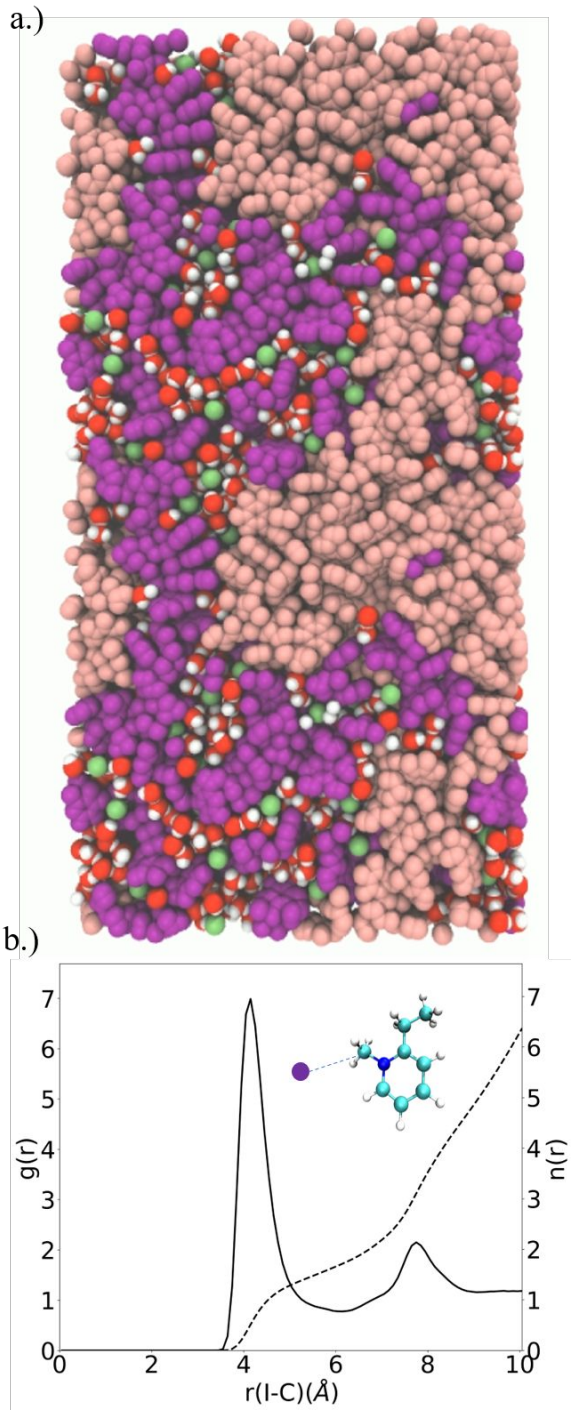

Figure 6. a.) Simulation snapshot for BCE, purple represents pyridine and pyridinium, pink is styrene, white and red correspond to water, and green is the iodide counterion. b.) The radial distribution function, g(r), (solid line) and coordination number, n(r), (dashed line) for the I^- distance from the $-CH_3$ group attached to N^+ (I-C) in the BCE.

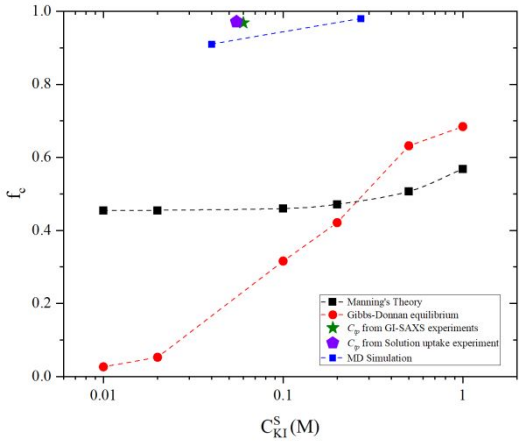

Figure 7. f_c determined from different experimental approaches and MD simulations.

the large values attained from **equation 5** – which derive from the identification of C_{tp}.

The MD simulations reveal that 90% of ion charge pairs in the BCE are not dissociated - namely they are solvated by counterion in the first solvation shell. This poor dissociation further supports the low activity of ions in the BCE. Additionally, the incorporation of KI salt to the simulated BCEs also showed additional iodide ions condensing on the BCE chain. This is an important observation as Manning's model (**equation 11**) assumes that all counterions from adsorbed salt are dissociated. Note: **Figure S5** provides a similar plot to **Figure 7** but the counterion contribution from adsorbed salt in Manning's theory is excluded (**equation S3**). f_c does not shift much if the counterion contribution from adsorbed salt is included.

It is clear that the MD simulations provide unique insights that are not possible via experimental techniques. More importantly, the MD simulations signal that there may not be two distinct classification of ions that are dissociated near or substantially below the Bjerrum length(4). Rather, it seems the extent of dissociation and activity may be governed by solvation and the uptake of water. To test this idea, a separate and idealized simulation was carried out where the BCE film was diluted significantly with water - 650 water molecules per ionic block. The f_c for the very dilute BCE chains in the MD simulation was 40% - which was substantially smaller. This simulation result highlights the importance for

breaking ion charge pairs in polymer electrolytes via solvation.

Previous results indicated that water uptake and solvation may be vital to describing the activity of ions in the thin BCE film. Thus, it was decided to perform ionic conductivity experiments under the following conditions: i.) the BCE film interfaced with liquid droplets with KI_{aq} and ii.) the BCE film, featuring adsorbed salt, under 95% relative humidity. The latter condition tested what might happen to ionic conductivity in the BCE thin film when starved of water (i.e., poor solvation). For the ionic conductivity experiments, it is important to note that the BCE thin films had the P2VP/NMP^+ I^- block as the majority block in terms of volume fraction. Hence, the ion conducting block was fairly percolated(32) so isolated ionic channels did not hinder ionic conductivity significantly.

Figure 8a reports the ionic conductivity of the PS*b*P2VP/NMP^+ I^- BCE thin film interfaced with liquid KI_{aq} solutions of varying concentrations. Ionic conductivity of the BCE thin film increased with increasing concentration of KI in the liquid solution because ionic conductivity is linearly proportional to the concentration of fixed charge carriers(2). **Figure S6a** highlights this point as the conductance of the KI_{aq} droplet without BCE film is provided. **Figures S6b-d** also shows the chamber for ionic conductivity measurements and representative Nyquist plots that were fitted with electric circuit equivalent models that were used to extract BCE film resistance values. **Figure 8b** reports the ionic conductivity of BCE thin films that contained adsorbed salt under 95% relative humidity. The x-axis in **Figure 8b** corresponds to the external liquid solution that the BCE film was exposed to for salt adsorption prior to removal of that liquid droplet and then testing the thin film BCE ionic conductivity under humidity control. The greater concentration of the KI_{aq} liquid exposed to the BCE film resulted in more salt adsorption (**Figure 4a**). Unexpectedly, the ionic conductivity decreased for a BCE film exposed to KI_{aq} greater than 0.01 M.

The drastic differences in ionic conductivity values and trends of the BCE film in **Figures 8a** and **8b** highlight the importance of water on ionic conductivity and dissociating ion charge pairs through solvation. Although **Figure 8a** shows an increase in ionic conductivity with an increase in external KI_{aq} concentration, it was decided to see what happens to the ionic conductivity data in **Figures 8a** and **8b** by normalizing the ionic conductivity data to the concentration of ionic groups in the BCE (both from the polymer and adsorbed salt). This normalized ionic conductivity term in the BCE is a proxy for the summation of the ionic mobility values within the BCE(2). **Figure 8c** plots the normalized conductivity data versus the number of water molecules per ionic group in the BCE film (λ). The amount of water in the BCE film hailed from QCM experiments (**Figure 2b** and **Figure S7**) while the concentration of ions in the film came from ion sorption and release experiments (**Figure 4a**).

Figure 8c accentuates the importance hydration has on ionic mobility in BCE films. With increased hydration, ion charge pairs are further dissociated and making it easier for counterions to migrate under electrochemical potential gradients. **Figure 8c** features two clusters of data that correspond to experiments under 95% relative humidity and the other under KI_{aq} liquid solutions. Although the magnitude of the values is drastically different, most data points show increasing normalized ionic conductivity with larger λ values. A drastic increase in ionic conductivity occurs between λ of 4.5 to 6. This large change in ionic conductivity with a modest change in λ will be explored in future studies. Recently, Nealey and de Pablo and co-workers (53) showed that increasing water contact in P2VP/NMP^+ homopolymers facilitates greater water-ion interactions that mediates ionic mobility. Figure 8c conveys that solvation via hydration is important for promoting dissociation of ion charge pairs and migration under applied electric fields.

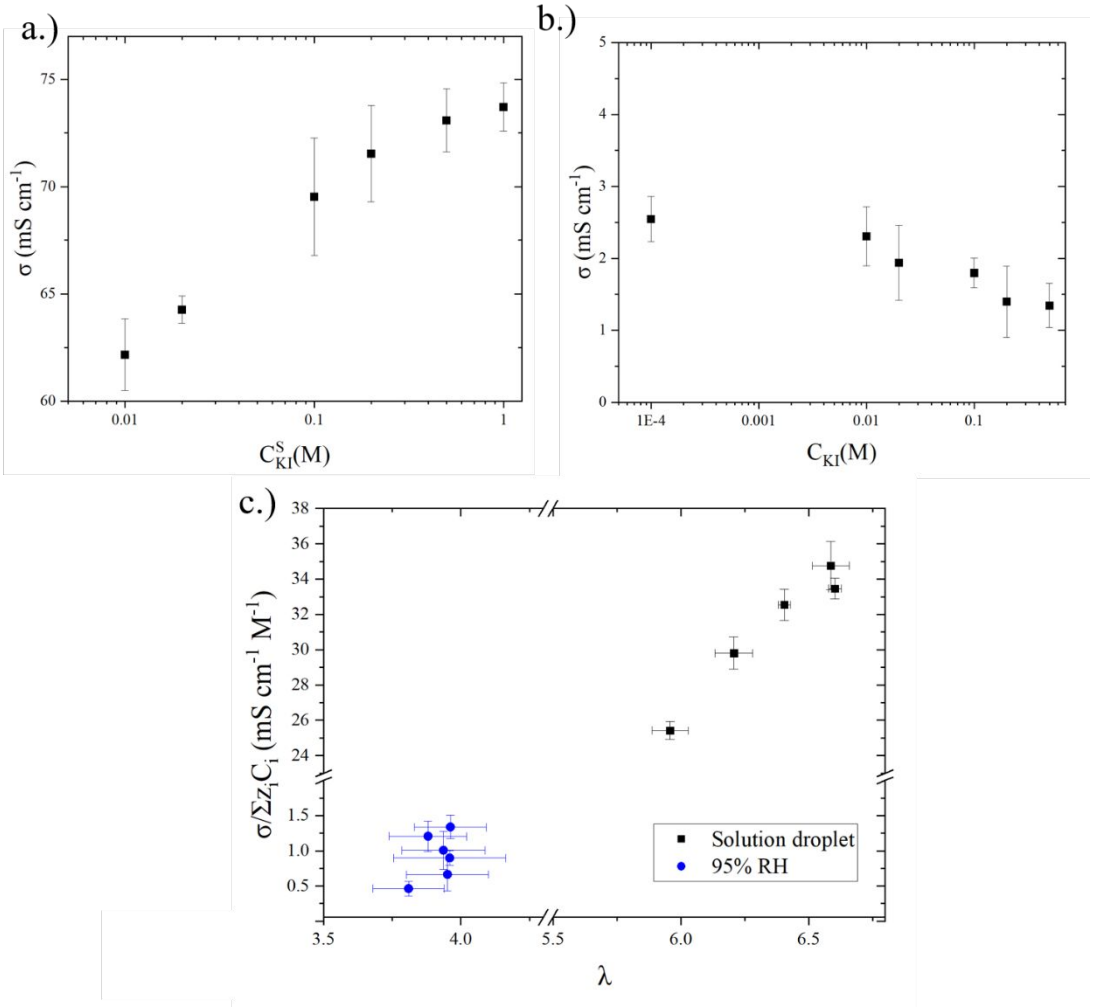

Figure 8. a.) Ionic conductivity of BCEs thin film with salt solution droplet on them; b.) Ionic conductivity of BCE thin films with adsorbed salt under 95% RH; c.). Normalized ionic conductivity versus λ (number of water molecules per ionic group) for the BCE thin films.

Finally, it is worth noting that the conductivity values from MD non-equilibrium simulations ranged from 25.9 - 46.4 mS cm^{-1} (**Table S1**). The simulations conveyed the same trend as a function of salt concentration as the experimental results with BCE films with liquid droplets (58 to 68 mS cm^{-1} – **Figure 8a**). The ionic conductivity from equilibrium simulations using the Nernst-Einstein equation (see SI section) were an order of magnitude smaller than those obtained by determining the instantaneous current from non-equilibrium simulations with an applied electric field (see **supplementary files 1** and **2** for simulation animations). Examination of the non-vehicular hopping of ions along the backbone revealed an order of magnitude of increase in the hopping rate with the application of an electric field. These simulation results clearly indicate the importance of non-vehicular hopping mechanism of ion transport along the backbone. Furthermore, examination of the distribution of the tetrahedral order parameter of water molecules (**Figure S8**) has revealed that the solvation structure of the water molecules themselves in the BCE systems deviates significantly from the bulk.

Figure 8c and MD simulations (**Table S1** and **Figure S8**) highlight the role solvation plays in ionic conductivity in BCEs. It is worth noting that the role of hydration, and its effect on f_c, is not captured explicitly in Manning's Theory of counterion condensation and the Gibbs-Donnan model. The ionic conductivity observations as a function of hydration (**Figure 8c**) are in line with previous studies that have examined ionic conductivity of PFSAs under various degrees of hydration(54, 55). Further, it is well-known that polymer electrolytes for lithium ion

batteries, which typically features no water, experience better ionic conductivity when they contain constituents that promote ion dissociation(55, 56).

CONCLUSIONS

A well-ordered model BCE, advanced metrology, and molecular simulations were brought together in concert to understand the low activity of ions in polymer electrolytes. Depending on the approach, there was discrepancy in the extent of counterion condensation (f_c). Because BCE thin films have a high concentration of fixed charge groups, they display low activity coefficients because the BCE cannot adsorb enough water due to the adjacent hydrophobic, glassy polystyrene block. Interestingly, the Gibbs-Donnan model shows that the majority of the ionic groups along the polymer backbone are exerting some level activity when the BCE is in the osmotic-controlled regime. In other words, there does not seem to be a large contingent of ions that are condensed along the polymer backbone not exerting activity. However, the Gibbs-Donnan model analysis does show that fixed charges along the polymer backbone do become screened through co-ion adsorption. This observation would explain the continuous deswelling of BCE film in the condensation-controlled regime in GI-SAXS and QCM experiments.

The implications of the simulation and experimental results highlight the importance of capturing water activity in the BCEs to understand the dissociation and activity of ions, and subsequently ionic conductivity and selectivity properties in nanostructured BCEs. Manning's Theory of counterion condensation was shown to predict the activity coefficients of ions in the BCE film with extraordinary accuracy provided the average distance between fixed charges was calculated correctly. However, Manning's Theory only captures the role of water on ion activity through the dielectric constant. The Gibbs-Donnan model takes into account water indirectly through the activity coefficient of ions in the BCE film. Future work is needed for models that capture water activity explicitly in polymer electrolytes in the context of understanding ion activity, migration, and selectivity. The role of solvation, rather than distinct populations of condensed and non-condensed counterions, (**Figure 9**) is posited to be a more appropriate molecular picture for understanding the extent of dissociated ion pairs in polymer electrolytes.

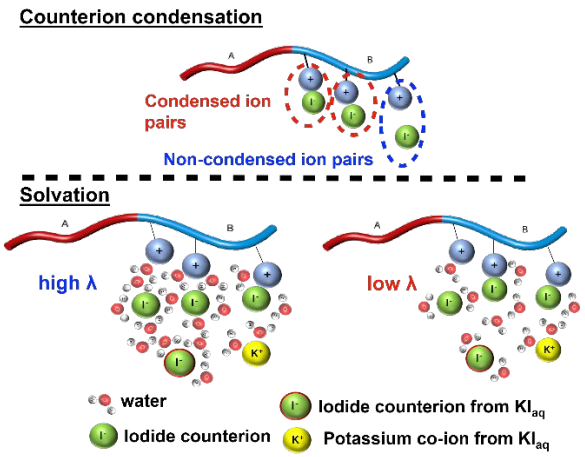

Figure 9. Illustration of counterion condensation in a BCE chain (top image) and solvated ion pairs in a BCE chain with different levels of hydration (bottom image).

AUTHOR CONTRIBUTIONS

Q.L. performed all experiments. D.B., J.S., and Q.Z. assisted with GI-SAXS experiments and reviewed the manuscript. S.K. fabricated IDEs and J.X. synthesized OH-random copolymer. J.L. assisted with the synthesis of OH-random copolymer and reviewed the manuscript. K. L. performed all MD simulations. Q.L., K.L., R.K., and C.G.A. designed the experiments, analyzed data, and wrote the manuscript.

DATA AVAILABILITY

Data are available at the request of the corresponding authors, R.K. and C.G.A.

ACKNOWLEDGEMENTS

This material is based upon work supported by the U.S. Department of Energy, Office of Science, Office of Basic Energy Sciences Separation Science program under Award Number DE-SC0018989. This research used resources of the Advanced Photon Source, a U.S. Department of Energy (DOE) Office of Science User Facility operated for the DOE Office of Science by Argonne National Laboratory under Contract No. DE-AC02-06CH11357 (Beamline 8-ID-E for GI-SAXS experiments). LSU Shared Instrumentation Facilities (electron

microscopy and LC-MS) and High-Performance Computing Facilities were used for this work. ICP-OES was made available from the Cain Department of Chemical Engineering at LSU. J.L. acknowledges startup funding from LSU. Special thanks to Daniel Willis at LSU for evaporating metals in the preparation of IDEs.

REFERENCES

1. Strathmann H, Grabowski A, Eigenberger G. Ion-Exchange Membranes in the Chemical Process Industry. Industrial & Engineering Chemistry Research. 2013;52(31):10364-79.
2. Sata T. Ion exchange membranes: preparation, characterization, modification and application: Royal Society of chemistry; 2007.
3. Kamcev J, Freeman BD. Charged Polymer Membranes for Environmental/Energy Applications. Annual Review of Chemical and Biomolecular Engineering. 2016;7:111-33.
4. Kamcev J, Paul DR, Freeman BD. Ion Activity Coefficients in Ion Exchange Polymers: Applicability of Manning's Counterion Condensation Theory. Macromolecules. 2015;48(21):8011-24.
5. Palakkal VM, Rubio JE, Lin YJ, Arges CG. Low-Resistant Ion-Exchange Membranes for Energy Efficient Membrane Capacitive Deionization. ACS Sustainable Chemistry & Engineering. 2018;6(11):13778-86.
6. Ramon GZ, Feinberg BJ, Hoek EMV. Membrane-based production of salinity-gradient power. Energy Environ Sci. 2011;4(11):4423-34.
7. Biesheuvel PM, van der Wal A. Membrane capacitive deionization. Journal of Membrane Science. 2010;346(2):256-62.
8. Capeci SW, Pintauro PN, Bennion DN. The molecular-level interpretation of salt uptake and anion transport in Nafion membranes. Journal of the Electrochemical Society. 1989;136(10):2876-82.
9. Geise GM. Experimental characterization of polymeric membranes for selective ion transport. Current Opinion in Chemical Engineering. 2020;28:36-42.
10. Guzman-Garcia AG, Pintauro PN, Verbrugge MW, Hill RF. Development of a space-charge transport model for ion-exchange membranes. AIChE Journal. 1990;36(7):1061-74.
11. Yang Y, Pintauro PN. Multicomponent Space-Charge Transport Model for Ion-Exchange Membranes with Variable Pore Properties. Industrial & Engineering Chemistry Research. 2004;43(12):2957-65.
12. Kamcev J, Galizia M, Benedetti FM, Jang ES, Paul DR, Freeman BD, et al. Partitioning of mobile ions between ion exchange polymers and aqueous salt solutions: importance of counter-ion condensation. Phys Chem Chem Phys. 2016;18(8):6021-31.
13. Kamcev J, Paul DR, Manning GS, Freeman BD. Predicting Salt Permeability Coefficients in Highly Swollen, Highly Charged Ion Exchange Membranes. ACS Appl Mater Interfaces. 2017;9(4):4044-56.
14. Beers KM, Hallinan DT, Wang X, Pople JA, Balsara NP. Counterion Condensation in Nafion. Macromolecules. 2011;44(22):8866-70.
15. Kamcev J, Paul DR, Freeman BD. Effect of fixed charge group concentration on equilibrium ion sorption in ion exchange membranes. Journal of Materials Chemistry A: Materials for Energy and Sustainability. 2017;5(9):4638-50.
16. Galizia M, Manning GS, Paul DR, Freeman BD. Ion partitioning between brines and ion exchange polymers. Polymer. 2019;165:91-100.
17. Peng J, Zawodzinski TA. Describing ion exchange membrane-electrolyte interactions for high electrolyte concentrations used in electrochemical reactors. Journal of Membrane Science. 2020;593:117340.
18. Kamcev J, Paul DR, Manning GS, Freeman BD. Accounting for frame of reference and thermodynamic non-idealities when calculating salt diffusion coefficients in ion exchange membranes. Journal of Membrane Science. 2017;537:396-406.
19. Kamcev J, Sujanani R, Jang E-S, Yan N, Moe N, Paul DR, et al. Salt concentration dependence of ionic conductivity in ion exchange membranes. Journal of Membrane Science. 2018;547:123-33.
20. Kamcev J, Doherty CM, Lopez KP, Hill AJ, Paul DR, Freeman BD. Effect of fixed charge group concentration on salt permeability and diffusion coefficients in ion exchange membranes. Journal of Membrane Science. 2018;566:307-16.
21. Kamcev J, Paul DR, Manning GS, Freeman BD. Ion Diffusion Coefficients in Ion Exchange Membranes:

Significance of Counterion Condensation. Macromolecules. 2018;51(15):5519-29.
22. Jang E-S, Kamcev J, Kobayashi K, Yan N, Sujanani R, Talley SJ, et al. Effect of Water Content on Sodium Chloride Sorption in Cross-Linked Cation Exchange Membranes. Macromolecules. 2019;52(6):2569-79.
23. Beers KM, Hallinan DT, Wang X, Pople JA, Balsara NP. Counterion Condensation in Nafion. Macromolecules. 2011;44(22):8866-70.
24. Kusoglu A, Weber AZ. New Insights into Perfluorinated Sulfonic-Acid Ionomers. Chemical Reviews. 2017;117(3):987-1104.
25. Colby RH, Boris DC, Krause WE, Tan JS. Polyelectrolyte conductivity. Journal of Polymer Science Part B: Polymer Physics. 1997;35(17):2951-60.
26. Bordi F, Colby RH, Cametti C, De Lorenzo L, Gili T. Electrical conductivity of polyelectrolyte solutions in the semidilute and concentrated regime: the role of counterion condensation. The Journal of Physical Chemistry B. 2002;106(27):6887-93.
27. Muthukumar M. Theory of counter-ion condensation on flexible polyelectrolytes: Adsorption mechanism. The Journal of Chemical Physics. 2004;120(19):9343-50.
28. Balastre M, Li F, Schorr P, Yang J, Mays JW, Tirrell MV. A Study of Polyelectrolyte Brushes Formed from Adsorption of Amphiphilic Diblock Copolymers Using the Surface Forces Apparatus. Macromolecules. 2002;35(25):9480-6.
29. Brettmann BK, Laugel N, Hoffmann N, Pincus P, Tirrell M. Bridging contributions to polyelectrolyte brush collapse in multivalent salt solutions. Journal of Polymer Science Part A: Polymer Chemistry. 2016;54(2):284-91.
30. Jackson NE, Brettmann BK, Vishwanath V, Tirrell M, de Pablo JJ. Comparing solvophobic and multivalent induced collapse in polyelectrolyte brushes. ACS Macro Letters. 2017;6(2):155-60.
31. Arges CG, Kambe Y, Suh HS, Ocola LE, Nealey PF. Perpendicularly Aligned, Anion Conducting Nanochannels in Block Copolymer Electrolyte Films. Chemistry of Materials. 2016;28(5):1377-89.
32. Arges CG, Kambe Y, Dolejsi M, Wu G-P, Segal-Pertz T, Ren J, et al. Interconnected ionic domains enhance conductivity in microphase separated block copolymer electrolytes. Journal of Materials Chemistry A. 2017;5(11):5619-29.
33. Arges CG, Li K, Zhang L, Kambe Y, Wu G-P, Lwoya B, et al. Ionic conductivity and counterion condensation in nanoconfined polycation and polyanion brushes prepared from block copolymer templates. Molecular Systems Design & Engineering. 2019;4(2):365-78.
34. Kambe Y, Arges CG, Czaplewski DA, Dolejsi M, Krishnan S, Stoykovich MP, et al. Role of Defects in Ion Transport in Block Copolymer Electrolytes. Nano Letters. 2019;19(7):4684-91.
35. Xiong S, Li D, Hur S-M, Craig GSW, Arges CG, Qu X-P, et al. The Solvent Distribution Effect on the Self-Assembly of Symmetric Triblock Copolymers during Solvent Vapor Annealing. Macromolecules. 2018;51(18):7145-51.
36. Kambe Y, Arges CG, Patel SN, Stoykovich MP, Nealey PF. Ion Conduction in Microphase-Separated Block Copolymer Electrolytes. The Electrochemical Society Interface. 2017;26(1):61-7.
37. Park MJ, Balsara NP. Phase Behavior of Symmetric Sulfonated Block Copolymers. Macromolecules. 2008;41(10):3678-87.
38. Polymeropoulos G, Zapsas G, Ntetsikas K, Bilalis P, Gnanou Y, Hadjichristidis N. 50th Anniversary Perspective: Polymers with Complex Architectures. Macromolecules. 2017;50(4):1253-90.
39. Ji S, Wan L, Liu C-C, Nealey PF. Directed self-assembly of block copolymers on chemical patterns: A platform for nanofabrication. Progress in Polymer Science. 2016;54-55:76-127.
40. Manning GS. Limiting laws and counterion condensation in polyelectroyte solutions. I. Colligative properties. Journal of Chemical Physics. 1969;51(3):924-33.
41. Guo Y, Liu Q, Peng C, Wang E, Joy A, Cakmak M. Colloid silica nanoparticles trapped morphology of polymer blends during solvent evaporation. European Polymer Journal. 2018;107:164-72.
42. Su Z, Kole S, Harden LC, Palakkal VM, Kim C, Nair G, et al. Peptide-modified electrode surfaces for promoting anion exchange ionomer microphase separation and ionic conductivity. ACS Materials Letters. 2019;1(4):467-75.
43. Arges CG, Wang L, Parrondo J, Ramani V. Best practices for investigating anion exchange membrane

suitability for alkaline electrochemical devices: case study using quaternary ammonium poly (2, 6-dimethyl 1, 4-phenylene) oxide anion exchange membranes. Journal of The Electrochemical Society. 2013;160(11):F1258.

44. Jiang Z, Li X, Strzalka J, Sprung M, Sun T, Sandy AR, et al. The dedicated high-resolution grazing-incidence X-ray scattering beamline 8-ID-E at the Advanced Photon Source. Journal of Synchrotron Radiation. 2012;19(4):627-36.

45. Jiang Z. GIXSGUI: a MATLAB toolbox for grazing-incidence X-ray scattering data visualization and reduction, and indexing of buried three-dimensional periodic nanostructured films. Journal of Applied Crystallography. 2015;48(3):917-26.

46. Jorgensen WL, Maxwell DS, Tirado-Rives J. Development and testing of the OPLS all-atom force field on conformational energetics and properties of organic liquids. Journal of the American Chemical Society. 1996;118(45):11225-36.

47. Jorgensen WL, Chandrasekhar J, Madura JD, Impey RW, Klein ML. Comparison of simple potential functions for simulating liquid water. The Journal of Chemical Physics. 1983;79(2):926-35.

48. Plimpton S. Fast parallel algorithms for short-range molecular dynamics. Sandia National Labs., Albuquerque, NM (United States); 1993.

49. Kankare J. Sauerbrey equation of quartz crystal microbalance in liquid medium. Langmuir. 2002;18(18):7092-4.

50. Peng J, Zawodzinski TA. Describing ion exchange membrane-electrolyte interactions for high electrolyte concentrations used in electrochemical reactors. Journal of Membrane Science. 2020;593.

51. Hamer WJ, Wu YC. Osmotic Coefficients and Mean Activity Coefficients of Uni-univalent Electrolytes in Water at 25°C. Journal of Physical and Chemical Reference Data. 1972;1(4):1047-100.

52. Shilov IY, Lyashchenko AK. Modeling activity coefficients in alkali iodide aqueous solutions using the extended Debye-Hückel theory. Journal of Molecular Liquids. 2017;240:172-8.

53. Chu W, Webb MA, Deng C, Colón YJ, Kambe Y, Krishnan S, et al. Understanding Ion Mobility in P2VP/NMP+ I–Polymer Electrolytes: A Combined Simulation and Experimental Study. Macromolecules. 2020.

54. Weber AZ, Newman J. Modeling transport in polymer-electrolyte fuel cells. Chemical reviews. 2004;104(10):4679-726.

55. Sepehr F, Liu H, Luo X, Bae C, Tuckerman ME, Hickner MA, et al. Mesoscale Simulations of Anion Exchange Membranes Based on Quaternary Ammonium Tethered Triblock Copolymers. Macromolecules. 2017;50(11):4397-405.

56. Savoie BM, Webb MA, Miller TF, 3rd. Enhancing Cation Diffusion and Suppressing Anion Diffusion via Lewis-Acidic Polymer Electrolytes. Journal of Physical Chemistry Letters. 2017;8(3):641-6.

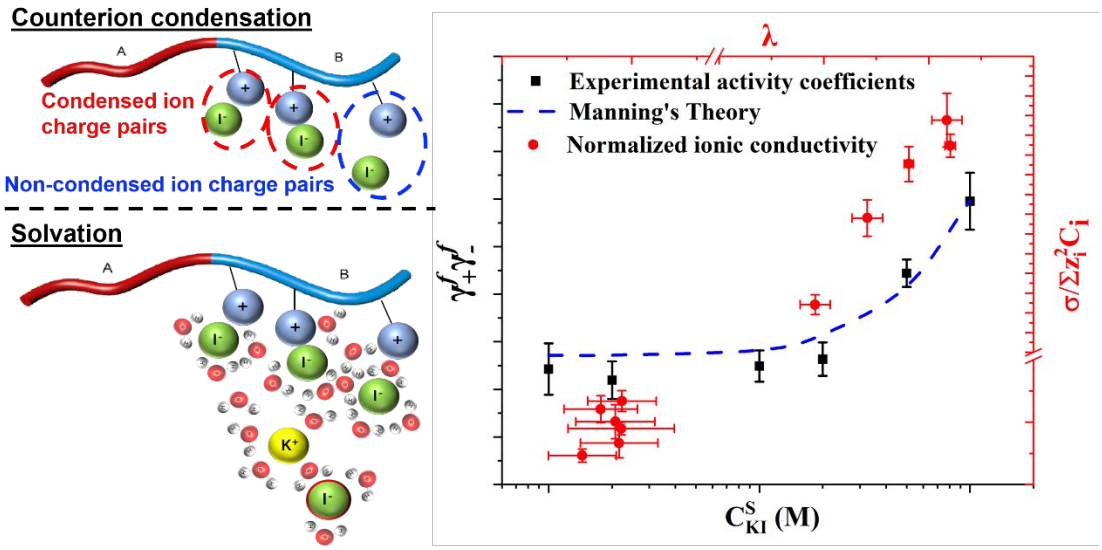

Dissociation of ion charge pairs in block copolymer electrolytes and its relation to activity coefficients and normalized ionic conductivity.